https://dx.doi.org/10.1016/j.jallcom.2018.07.372

Phase field modeling of Widmanstätten ferrite formation in steel

Chen Lin, Jianquan Wan, Haihui Ruan*
Department of Mechanical Engineering, The Hong Kong Polytechnic University
Hung Hom, Kowloon, Hong Kong, China

Abstract

Widmanstätten Ferrite (WF) formation is a complex transformation process, in which various physical variables are involved. In this work, we propose a phase field model of WF formation, which involves the interfacial anisotropy, misfit strain and multicomponent diffusion, for comprehending their coupled effects. The Fe-N-C system is adopted in numerical simulation and the realistic thermodynamic parameters are used. Attention is paid to growth speed and radius of the WF tip, which are dependent on the strength of anisotropic interfacial energy, eigenstrain, concentration and temperature. The simulation results reveal the individual effect of each of these variables and that none of the separate effect can be strong enough to achieve the large aspect ratio of Widmanstätten pattern. The morphology should be the result of their combined effect, which is not a simple linear super-position.

Keyword*: Phase field Modeling; Widmanstätten ferrite formation; Interfacial Anisotropy; Misfit strain; Multicomponent.*

1. Introduction

The physical and mechanical properties of an engineering material are significantly affected by the phase volume fraction and morphology. Therefore, it has been recognized that effectively controlling the phase volume fraction and morphology of a material can improve the performance of existing materials or lead to the development of new materials. The transformation from austenite to ferrite is one of the most important structural transitions in cooling steels. Different ferrite morphologies can be precipitated from the undercooled austenite, significantly affecting mechanical properties. Widmanstätten ferrite (WF) is one of the most interesting and important morphologies. It typically occurs below the A_{e3} temperature and plays a dominant role in toughening steel. Understanding the mechanism of WF formation is thus important for optimization and development of steels.

Theoretical studies were first conducted by Zener [1] and Hillert et al. [2], in which the Gibbs-Thomson equation was proposed to analyze the growth kinetics of spherical particles in an infinite solid solution. The lengthening rate of WF was then predicted theoretically by Trivedi et al. [3] by considering the interface kinetics and surface tension. A more effective model was proposed by Townsend and Kirkaldy [4], in which the Zener–Hillert theory was combined with the Mullins-Sekerka model [5], to investigate the spacing and lengthening rate of WF plates. These theoretical models are limited by assumptions required to make the diffusion problem with a migrating interface analytically solvable. For example, the local equilibria of the concentrations at the interface and paraboloid-shaped precipitates must be assumed.

A phase transformation is generally coupled with various physical processes, such as

* Corresponding author Tel.: + 852 2766 6648, Fax: +852 2365 4703, E-mail address: haihui.ruan@polyu.edu.hk

diffusion, interface migration, morphology evolution, thermal conduction, and mechanical deformation. Because these processes are intertwined, it is difficult to determine their respective influences using only experimental and analytical studies. Thus, numerical methods, e.g. the phase field approach, have been proposed and rapidly developed in the last two decades to become powerful tools for the quantitative analysis of phase transformations in materials. The phase field method employs a diffusive interface description [6], which makes it a powerful technique for dealing with complex morphologies without making any a priori assumptions about the shape of the interface. Across the diffusive interface, field variables vary continuously from one uniform value corresponding to a certain type of phase or domain to a different uniform value corresponding to another phase or domain. Instead of defining a moving boundary condition, the interface movement and microstructure evolution is implicitly described by the temporal evolution of the phase field variables. By coupling the effects of processes including thermal conduction, elemental diffusion, and mechanical deformation induced by lattice mismatch or applied stress, and the chemical reactions, the phase field method can be extended and utilized across many fields of materials science [7-12].

A few applications of the phase field approach for WF formation have been proposed. In these studies, the interfacial energy is assumed to be highly anisotropic, and depends strongly on the orientation of the phase boundary. The tip of the Widmanstätten plate is an incoherent interface that has a much higher interfacial energy than the coherent interfaces at the sides. The thickness of the interface also varies due to this anisotropy: the coherent interface is much thinner than the incoherent interface. Loginova *et al*. [13] investigated WF formation by introducing a regularized gradient energy coefficient to describe the strong interfacial anisotropy. Based on this approach, Yamanaka *et al*. [14] investigated even wider range of interfacial anisotropy and obtained a very sharp Widmanstätten tip, which is in agreement with experimental observations. The misfit strain induced by the mismatch of lattice parameters between the newly formed phase and the matrix also plays an important role in determining the phase morphology [15], which was first demonstrated in the study of precipitate formation in Ni-based alloys [16]. Recently, Cottura *et al*. [17-18] determined that the misfit strain also significantly affects the morphology of WF. Zhang *et al*. [19] then adopted the phase field model by Cottura *et al* [17-18] to investigate WF formation in an Fe-C alloy with more realistic physical parameters.

Previous investigations have shown that the Widmanstätten pattern can be caused by either interfacial anisotropy or misfit strain, and that variation in the compositions of the α and γ phases also affects the growth kinetics of WF. In these studies, the steel is considered a binary alloy, and thus diffusion of multiple components is not included. However, most steels contain multiple components, and other added alloying elements can sometimes play a more dominant role than carbon. To explore the coupled effects of all these factors, this study present proposes a phase-field model that includes them. A numerical simulation based on the Fe-C-N system is then conducted, which comprehensively reflects the effects of interfacial anisotropy, anisotropic elasticity, and multicomponent diffusion on Widmanstätten formation. By varying the magnitudes of the strength of the anisotropic interfacial energy, eigenstrain,

concentration and temperature, the Widmanstätten growth, as characterized by the tip velocity and radius of curvature, can be analyzed.

2. Methodology

2.1. Gibbs Free Energy Formulation

Based on the Ginzburg-Landau formulation [20] and the diffuse-interface approach, the total Gibbs free energy, including the effect of interface anisotropy, misfit strain, multiple alloy elements and temperature, can be expressed as follows:

$$F = \int_{\Omega} \left[f\left(\phi, u^1 \ldots u^n, \mathbf{d}, T\right) + \frac{\lambda^2}{2} \left|\nabla \phi\right|^2 \right] dV , \tag{1}$$

where F is the total Gibbs free energy in a closed system Ω; f is the bulk energy density per unit volume; ϕ is the phase order parameter, which is defined as 1 for ferrite and 0 for austenite; u^i (i = 1…n) represents the component concentration of alloying element i, defined as the mole ratio of the alloying element, i, to iron; and T is the absolute temperature. Owing to the lattice mismatch between the newly formed α phase and the matrix γ phase, considerable eigenstrains result during the $\gamma \rightarrow \alpha$ transformation. As a result of the constraint of the surrounding γ matrix, these eigenstrains give rise to a significant deformation field, **d**, and contribute strain energy to the bulk energy [17-19], f, as expressed in Eq. (1). The interfacial energy density is represented by $\lambda^2 \left|\nabla \phi\right|^2 / 2$, where ∇ is the gradient operator, and λ is a scale factor for the interfacial energy density.

Following Kim *et al.* [21], the bulk energy density, f, is defined as the summation of the weighted average of the energy densities in α and γ, as follows:

$$f = p(\phi) f^{\alpha}\left(\phi, u^1 \ldots u^n, \mathbf{d}, T\right) + \left[1 - p(\phi)\right] f^{\gamma}\left(\phi, u^1 \ldots u^n, \mathbf{d}, T\right) + Wq(\phi) , \tag{2}$$

where f^{α} and f^{γ} are the bulk energy densities in the α and γ phases, respectively, and $p(\phi)$ is the weighting function, which has the form of $p(\phi) = \phi^3(10\text{-}15\phi\text{+}6\phi^2)$. The double-well potential, $Wq(\phi)$, is used to describe the energy barrier between neighboring phases during the phase transformation, in which W is the height of the energy barrier and is related to the interfacial energy (per unit area), σ, and the interfacial thickness, δ, by the expression $W=18\sigma/\delta$ [22]. The double-well function, $q(\phi)$, has minima at $\phi = 1$ and $\phi = 0$, is symmetric about $\phi = 0.5$, and is expressed in the form of $q(\phi) = \phi^2(1\text{-}\phi)^2$.

Assuming that the contributions of chemical diffusion and mechanical deformation are decoupled, the bulk energy density can be expressed as follows:

$$f^{\alpha(\text{or}\,\gamma)} = f_{\text{chem}}^{\alpha(\text{or}\,\gamma)}\left(u^1 \ldots u^n, T\right) + f_{\text{mech}}^{\alpha(\text{or}\,\gamma)}\left(\mathbf{d}\right) , \tag{3}$$

where $f_{\text{chem}}^{\alpha(\text{or}\,\gamma)}$ is the chemical energy per unit volume, described based on the Hillert Staffansson approach (see Appendix A or [23]), and $f_{\text{mech}}^{\alpha(\text{or}\,\gamma)}$ is the strain energy density, expressed as follows:

$$f_{\text{mech}}^{\alpha(\text{or }\gamma)} = \frac{1}{2}\left(\boldsymbol{\varepsilon}_{\alpha(\text{or }\gamma)}^{\text{e}T} \cdot \left(\mathbf{D}_{\alpha(\text{or }\gamma)}^{\text{e}} \boldsymbol{\varepsilon}_{\alpha(\text{or }\gamma)}^{\text{e}}\right)\right), \tag{4}$$

where $\mathbf{D}_{\alpha(\text{or }\gamma)}^{\text{e}}$ is the stiffness matrix of the α or γ phase, and $\boldsymbol{\varepsilon}_{\alpha(\text{or }\gamma)}^{\text{e}}$ is the elastic strain tensor in the α or γ phase. Assuming elastic deformation, the elastic strain can be obtained as follows:

$$\boldsymbol{\varepsilon}_{\alpha}^{\text{e}} = \boldsymbol{\varepsilon} - \boldsymbol{\varepsilon}^{\text{g}},\ \boldsymbol{\varepsilon}_{\gamma}^{\text{e}} = \boldsymbol{\varepsilon}, \tag{5}$$

where $\boldsymbol{\varepsilon}^{\text{g}}$ is the anisotropic eigenstrain tensor, describing the lattice mismatch between the α and γ phases, as given in [17-19], and $\boldsymbol{\varepsilon}$ is the total strain derived from geometric relation under the assumption of small deformation, as follows:

$$\boldsymbol{\varepsilon} = \left\{\varepsilon_{ij}\right\} = \left\{\frac{1}{2}\left(\frac{\partial u_i}{\partial x_j} + \frac{\partial u_j}{\partial x_i}\right)\right\}\ \left(i = 1,2,3;\ j = 1,2,3\right). \tag{6}$$

Ignoring the body force, the equilibrium equation can be expressed as:

$$\text{div}\left(\boldsymbol{\sigma}\right) = 0, \tag{7}$$

where div is the divergence operator, and $\boldsymbol{\sigma}$ is the stress tensor. The stress tensor is defined as $\boldsymbol{\sigma} = \mathbf{D}^{\text{e}}\boldsymbol{\varepsilon}^{\text{e}}$, where $\mathbf{D}^{\text{e}}$ and $\boldsymbol{\varepsilon}^{\text{e}}$ for the phase field are expressed as follows:

$$\mathbf{D}^{\text{e}} = p\left(\phi\right)\mathbf{D}_{\alpha}^{\text{e}} + \left[1 - p\left(\phi\right)\right]\mathbf{D}_{\gamma}^{\text{e}} \tag{8a}$$

$$\boldsymbol{\varepsilon}^{\text{e}} = p\left(\phi\right)\boldsymbol{\varepsilon}_{\alpha}^{e} + \left[1 - p\left(\phi\right)\right]\boldsymbol{\varepsilon}_{\gamma}^{e} = \boldsymbol{\varepsilon} - p\left(\phi\right)\boldsymbol{\varepsilon}^{\text{g}} \tag{8b}$$

The interfacial energy is given by $\lambda^2\left|\nabla\phi\right|^2/2$ in Eq. (1). If the interface is isotropic with an energy density (per unit area), σ, and interface thickness, δ, then $\lambda^2 = \sigma\delta$ [22]. For WF, the interfacial energy is considered to be highly anisotropic. The tip of the Widmanstätten plate is regarded as an incoherent interface with very high interfacial energy, whereas both sides of the Widmanstätten plate are assumed to be coherent interfaces that have lower interfacial energies. The thickness of the interface is also anisotropic: the coherent interfaces can be much thinner than the incoherent interfaces. The anisotropic interfacial energy and thickness are expressed as $\sigma = \sigma_0\eta(\theta)$ and $\delta = \delta_0\eta(\theta)$, respectively. Following Yamanaka *et al.* [14], the anisotropic function, $\eta(\theta)$, is expressed as follows:

$$\eta\left(\theta\right) = \begin{cases} \dfrac{1 + a\cos\left(2\theta_{\text{m}}\right)}{\cos\left(\theta_{\text{m}}\right)}\cos\left(\theta - \theta_0\right) & -\theta_{\text{m}} < \theta < \theta_{\text{m}} \\ -\dfrac{1 + a\cos\left(2\theta_{\text{m}}\right)}{\cos\left(\theta_{\text{m}}\right)}\cos\left(\theta - \theta_0\right) & -\pi - \theta_{\text{m}} < \theta < -\pi + \theta_{\text{m}} \\ -\dfrac{1 + a\cos\left(2\theta_{\text{m}}\right)}{\cos\left(\theta_{\text{m}}\right)}\cos\left(\theta - \theta_0\right) & \pi - \theta_{\text{m}} < \theta < \pi + \theta_{\text{m}} \\ 1 + a\cos\left(2\left(\theta - \theta_0\right)\right) & \text{other} \end{cases}, \tag{9}$$

where a is the strength of the interfacial anisotropy, θ_0 represents the fastest growth direction, and θ_m is a constant which can be determined by solving the equation $\eta(\theta_m)\sin(\theta_m)+\eta'(\theta_m)\cos(\theta_m) = 0$, where $\eta'(\theta) = d\eta(\theta)/d\theta$.

2.2. Evolution Equation

The non-conserved order parameter, ϕ, is governed by the Allen-Cahn equation [24]:

$$\partial\phi/\partial t = -M_\phi\left(\delta F/\delta\phi\right) = M_\phi\left\{\sigma_0\delta_0\left(\eta^2\nabla^2\phi - \frac{\partial}{\partial x}\left(\eta\eta'\frac{\partial\phi}{\partial y}\right) + \frac{\partial}{\partial y}\left(\eta\eta'\frac{\partial\phi}{\partial x}\right)\right) - \frac{\partial f}{\partial\phi}\right\}, \tag{10}$$

This indicates that the change in ϕ is along the gradient direction in the free energy landscape of $F(\phi)$. In Eq. (10), the coefficient M_ϕ is related to the interfacial mobility, and can be expressed in the form of $M_\phi = \varsigma M/\delta_0$ [13], where ς is a coefficient, and M is the interfacial mobility, which is assumed to be isotropic for simplicity in this model following Refs. [13-14].

Employing the conditionn that the total mass is conserved, the evolution of the fraction of component k, u^k, is given as follows:

$$\partial u^k/\partial t = -\nabla\cdot J_k, \tag{11}$$

where J_k is the diffusion flux of component k. Based on the Onsager linear law [25], J_k can be expressed as follows:

$$J_k = -\left(\sum_{j=1}^{n}\sum_{i=1}^{n}\left(L_{ki}\frac{\partial^2 f}{\partial u^i\partial u^j}\nabla u^j\right) + \sum_{i=1}^{n}\left(L_{ki}\frac{\partial^2 f}{\partial u^i\partial\phi}\right)\nabla\phi\right), \tag{12}$$

where u^i and u^j are the fractions of components i and j, respectively, in the n-component system. L_{ki} is a parameter related to the diffusional mobility and is expressed as follows:

$$L_{ki} = u^k y_{va} M_{ki}, \tag{13}$$

where y_{va} is the fraction of vacant interstitials, and M_{ki} is the diffusional mobility of component k affected by the ith component. The fraction of vacant interstitials, y_{va}, is expressed as follows:

$$y_{va} = p(\phi)\left(1 - \frac{1}{3}\sum_{i=1}^{n}u^i\right) + \left(1-p(\phi)\right)\left(1-\sum_{i=1}^{n}u^i\right), \tag{14}$$

M_{ki} is expressed as follows:

$$M_{ki} = \left(M_{ki}^{\alpha}\right)^{p(\phi)}\left(M_{ki}^{\gamma}\right)^{1-p(\phi)}, \tag{15}$$

where M_{ki}^{α} and M_{ki}^{γ} are the diffusional mobility of component k affected by the ith component in the α and γ phases, respectively.

Substituting Eqs. (2–3) into Eq. (10), Eqs. (12-15) into Eq. (11), and Eqs. (4, 5, 6, 8a, 8b) into Eq. (7) yields the governing equations for the order parameter, ϕ, the alloy element

fraction, u^{k}, and displacement, **d**, which are given in Eqs. (16a, 16b, and 16c), respectively:

$$\frac{\partial \phi}{\partial t} = M_{\phi}\left\{\begin{array}{l}\sigma^0\delta^0\left(\eta^2\nabla^2\phi - \dfrac{\partial}{\partial x}\left(\eta\eta'\dfrac{\partial \phi}{\partial y}\right) + \dfrac{\partial}{\partial y}\left(\eta\eta'\dfrac{\partial \phi}{\partial x}\right)\right) - \\ \dfrac{\partial p(\phi)}{\partial \phi}\left(f^{\alpha}_{\mathrm{chem}} + f^{\alpha}_{\mathrm{mech}} - f^{\gamma}_{\mathrm{chem}} - f^{\gamma}_{\mathrm{mech}}\right) - W\dfrac{\partial q(\phi)}{\partial \phi}\end{array}\right\}, \tag{16a}$$

$$\frac{\partial u^{\mathrm{k}}}{\partial t} = \nabla\cdot\left(u^{\mathrm{k}} y_{\mathrm{va}}\left(\begin{array}{l}\displaystyle\sum_{\mathrm{j}=1}^{\mathrm{n}}\sum_{\mathrm{i}=1}^{\mathrm{n}}\left(\left(M^{\alpha}_{\mathrm{ki}}\right)^{p(\phi)}\left(M^{\gamma}_{\mathrm{ki}}\right)^{1-p(\phi)}\frac{\partial^2 f}{\partial u^{\mathrm{i}}\partial u^{\mathrm{j}}}\nabla u^{\mathrm{j}}\right) + \\ \displaystyle\sum_{\mathrm{i}=1}^{\mathrm{n}}\left(\left(M^{\alpha}_{\mathrm{ki}}\right)^{p(\phi)}\left(M^{\gamma}_{\mathrm{ki}}\right)^{1-p(\phi)}\frac{\partial^2 f}{\partial u^{\mathrm{i}}\partial \phi}\right)\nabla\phi\end{array}\right)\right) \tag{16b}$$

and

$$\mathrm{div}\left[\left(p(\phi)\mathbf{D}^{\mathrm{e}}_{\alpha} + \left[1-p(\phi)\right]\mathbf{D}^{\mathrm{e}}_{\gamma}\right)\left(\left\{\frac{1}{2}\left(\frac{\partial d_i}{\partial x_j} + \frac{\partial d_j}{\partial x_i}\right)\right\} - p(\phi)\boldsymbol{\varepsilon}^{\mathrm{g}}\right)\right] = 0, \tag{16c}$$

By defining the reference length, l, reference time, $t_{\mathrm{ref}} = l^2/(RTM^{\alpha}_{\mathrm{CC}})$, and reference energy density per mole, $f_{\mathrm{ref}} = V_{\mathrm{m}}RT$, in which M^{α}_{CC}, V_{m}, and R are the diffusional mobility of carbon in the α phase, the molar volume of substitutional atoms, and the ideal gas constant, respectively, the non-dimensional evolution equations can then be derived for the numerical simulation (see Appendix B).

3. Numerical Analysis

As the three dimensions (3D) geometry of Widmanstätten ferrite observed experimentally is lath-shaped, the effect of the out-of-lath-plane curvature is ignored. The numerical investigation of WF formation was constrained in two dimensions (2D), and the simulation model is a 0.2 μm × 0.5 μm box, as shown in Fig. 1. The initial α phase is assumed to be an ellipse within the γ matrix. The semi-major and semi-minor axes are set to 20 nm and 30 nm. Owing to symmetry, one half of the elliptical α phase is modeled in the numerical simulation.

Fig. 1

The Fe-N-C system is adopted to account for the multicomponent chemical kinetics and diffusion. The thermodynamic parameters are based on realistic values (see Appendix A or [23]), and the initial carbon and nitrogen concentrations are defined as $u^{\mathrm{C}} = u^{\mathrm{N}} = 0.001$ in the α phase and $u^{\mathrm{C}} = u^{\mathrm{N}} = 0.01$ and in the γ phase. The initial displacements are set to zero throughout the entire domain. Zero-flux boundary conditions are applied to all sides for the phase and concentration evolution. Owing to the symmetry, the displacement in the Y-direction is constrained at the bottom side and the displacement in the X-direction is constrained along the axis (the left side), as shown in Fig. 1. All other boundaries are zero-flux for the displacement. The parameters for the phase interface and mechanical properties are listed in Table 1. For the simulation, the reference length, l, is 2 nm (i.e., $1/5\delta_0$), and the reference time, t_{ref}, is 0.51733 μs. COMSOL Multiphasic [26] is used to solve the governing equations based on the finite element method. To guarantee convergence of the solution, the calculation domain is discretized by uniform square mesh with a size of 0.5 nm

(i.e., $l/4$), and the initial and maximum time step are both $t_{ref}/30$ for temporal integration.

Table 1 Material properties used for numerical simulation with the proposed phase field model

3.1 Coupled Effects of the Interfacial Anisotropy and Misfit Strain

The morphology of WF after annealing for 1200μs at 930K is shown in Fig 2, in which a small strength of the interfacial anisotropy, $a = 0.2$, and eigenstrain, $\varepsilon_{11}^{g} = 0.04$, are considered. It can be observed that the initial ellipse of the α phase becomes needle-like, with a very sharp tip. The aspect ratio of the WF is approximately 12 at 1200 μs, which is within the realistic range (10–100) of experimental observation. When only the interfacial anisotropy with, $a = 0.2$, is considered, the WF formed after 1200 μs is shown in Fig. 2(b), and has an aspect ratio of only 1.5. If only the eigenstrain, $\varepsilon_{11}^{g} = 0.04$, is considered, the WF phase has an aspect ratio of 5 at 1200 μs, as shown in Fig. 2(c). These results indicate that neither the interfacial anisotropy nor the misfit strain alone is the primary cause of the very sharp and thin WF phase observed experimentally. The large aspect ratio of WF is thus the result of their combined effects and their combination is not a simple linear superposition. While interfacial anisotropy leads to a high-energy and thick interface at the WF tip, the heterogeneous elastic strain energy induced by the anisotropic eigenstrain leads to the highly orientated growth of WF. A high stress concentration occurs at the tip, resulting in a considerable value for the elastic strain energy, as shown in Fig. 3(a). In contrast, the stress level is very low along both sides of the WF phase, leading to a relatively low elastic energy, as shown in Fig. 3(b). The time-dependence of the elastic energy at the tip and sides of the WF phase are plotted in Fig. 3(c), and changes very slowly during the growth of Widmanstätten ferrite.

Fig. 2

Fig. 3

During the phase transformation, alloying elements are released from the newly formed ferrite and diffuse into the austenite matrix. This process results in elemental accumulation at the interface, suppressing the phase growth. At the Widmanstätten tip, the high free energy of the interface between the α phase and the matrix γ phase leads to more rapid diffusion and less accumulation. The carbon and nitrogen concentrations at 300 μs along the Y-axis (passing the Widmanstätten tip) and the X-axis (perpendicular to the side) are shown in Fig. 4(a) and (b), respectively. At the tip of the WF plate, the accumulation of carbon and nitrogen, indicated by the maximum concentrations shown in Fig. 4(a), are $u_{\max}^{C} = 0.0112$ and $u_{\max}^{N} = 0.0121$, respectively. The diffusion lengths, l_{diff}, of carbon and nitrogen, as defined in Fig. 4(a), are 10 nm and 7.5 nm, respectively. Along the side of the WF plate, the accumulation of carbon and nitrogen is larger ($u_{\max}^{C} = 0.0197$ and $u_{\max}^{N} = 0.0243$) and the diffusion lengths are longer ($l_{diff} \approx 28$ nm for carbon, and $l_{diff} \approx 19$ nm for nitrogen), as shown in Fig. 4(b). The variations in the diffusion length, l_{diff}, and the elemental accumulations,

$u_{\max}$, with time are further illustrated in Fig. 4(c) and (d) respectively. It is noted that the elemental accumulation and the diffusion length along the side of the WF increase with time, which prevents thickening of the WF plate. Consequently, the thickening of the WF plate is more diffusion-controlled. In contrast, l_{diff} and $u_{\max}^{\text{C or N}}$ at the tip remain unchanged, or even decrease slightly with time, which promotes sharpening at the tip.

Fig. 4

Because the elastic strain energy at the Widmanstätten tip changes very slowly, as shown in Fig. 3(c) and the elemental accumulation is insignificant, as shown in Fig. 4(d), the driving force, leading to the migration of interface along the Y-axis, could be assumed to be constant. The relationship between the tip velocity and driving force can be expressed as follows [28]:

$$V_{\text{n}} = \lambda\left[K_0\Delta f - K_1\left(\lambda + \frac{\partial^2\lambda}{\partial\theta^2}\right)\kappa\right] \tag{17}$$

where K_0 and K_1 are constants; Δf is the driving force, which can be expressed as $\Delta f = f_{\text{chem}}^{\alpha} + f_{\text{mech}}^{\alpha} - f_{\text{chem}}^{\gamma} - f_{\text{mech}}^{\gamma}$ in this study, and κ is the interfacial curvature. Considering the anisotropic interfacial function, $\lambda = (\sigma_0\delta_0)^{1/2}(1+2a\cos[(\theta-\theta_0)])$, the velocity of the Widmanstätten tip can be obtained as follows:

$$V_{\text{n}}^{\text{tip}} = \sqrt{\sigma_0\delta_0}\,(1+a)\left\{K_0\Delta f - K_1\sqrt{\sigma_0\delta_0}\,(1-3a)\,\kappa^{\text{tip}}\right\} \tag{18}$$

Eq. (18) leads to a constant growth rate at the Widmanstätten tip. For the case exemplified in Fig. 2(a), the tip velocity is 0.254×10^{-3} m/s, as shown in Fig. 5(a), which is in line with the experimental observations (the experimental value is 0.2×10^{-3} m/s) [29], and indicates that the lengthening of the WF plate can well be approximated by the 1-D model (Eq. (18)). In comparison, the width of the Widmanstätten ferrite increases much more slowly and parabolically with time, as shown in Fig. 5(b), due to the retarding effect of increasing elemental accumulation, as shown in Fig. 4(c) and (d).

Fig. 5

Associated with the nearly constant velocity and driving force of the tip growth, the radius of the tip curvature also remains unchanged during phase growth, as shown in Fig. 6. It can be observed that the tip curvature radius is unchanged during Widmanstätten ferrite growth, after an initial very rapid decrease. The tip curvature radius evolution for different initial morphologies are compared in Fig. 6. It is noted that the tip curvature radius is independent of the initial morphology, as illustrated by the three examples shown in Fig. 6.

Fig. 6

Eq. (18) is the 1-D solution for the tip velocity, which depends on the elastic strain energy density and the interfacial anisotropy. To elaborate these effects further, numerical studies are carried out using different anisotropy parameters. Because the eigenstrain induced by the $\gamma\rightarrow\alpha$ transformation has not been precisely measured, the eigenstrain, $\varepsilon_{11}^{\text{g}}$, is varied in the range of 0.0–0.10 (Note that $\varepsilon_{11}^{\text{g}}$ has been assumed to have a larger range in literature. For

example, it is in the range of 0.03–0.05 in Ref. [17] but 0.17 in Ref. [19]). The factor for interfacial anisotropy, a, is varied in the range of 0–0.6, which is in accordance with the previous study [14]. The dimensionless tip radius, r/r^0 (r^0 = 1 nm), with the interfacial anisotropy factor, a, and the eigenstrain, ε_{11}^{g}, is shown in Fig. 7(a). When a and ε_{11}^{g} are both small, the decrease in tip radius with decrease in both factors is approximately linear, while when the two factors are larger, the tip radius decreases faster with a nonlinear evolution law. It indicates that the morphology of WF tip is the result of nonlinear coupling effect of eigenstrain, ε_{11}^{g}, and interfacial anisotropy factor, a, rather than their simple linear super-position. According to Eq. (18), the tip velocity scales with the change in free energy density, Δf, and the tip curvature, $(1/r)$. Because Δf scales with a and $(\varepsilon_{11}^{g})^2$, the tip velocity is plotted against a and $(\varepsilon_{11}^{g})^2$ in Fig. 7(b). The results clearly show that when a and ε_{11}^{g} are relativly large, the tip velocity increases linearly with $(\varepsilon_{11}^{g})^2$ and a, which is in line with the prediction of Eq. (18).

Fig. 7

3.2 Effect of Chemical Kinetics

Chemical kinetics refers to time-dependent change driven by the degree of non-equilibrium, and can be achieved by varying the degree of undercooling and the elemental concentrations in the α and γ phases. First, the effect of elemental concentration is investigated based on the ratio of the initial concentration to the equilibrium concentration, given as:

$$\Omega_{\mathrm{C(or\ N)}}^{\alpha(\mathrm{or}\ \gamma)} = \left(u^{\mathrm{C(or\ N)}}\right)_{\mathrm{ini}}^{\alpha(\mathrm{or}\ \gamma)} \Big/ \left(u^{\mathrm{C(or\ N)}}\right)_{\mathrm{eq}}^{\alpha(\mathrm{or}\ \gamma)}, \tag{19}$$

where $\left(u^{\mathrm{N(or\ C)}}\right)_{\mathrm{ini}}^{\alpha(\mathrm{or}\ \gamma)}$ and $\left(u^{\mathrm{N(or\ C)}}\right)_{\mathrm{eq}}^{\alpha(\mathrm{or}\ \gamma)}$ are the initial and equilibrium concentrations, respectively, of carbon or nitrogen in the α or γ phase. A schematic diagram of the chemical energy density of the Fe-C-N solid solution for the α and γ phases is shown in Fig. 8, in which the equilibrium concentrations of carbon and nitrogen are close to the concentrations at the local minimum of the chemical energy density, i.e., $\left(u^{\mathrm{N(or\ C)}}\right)_{\mathrm{eq}}^{\alpha(\mathrm{or}\ \gamma)} \cong \left(u^{\mathrm{N(or\ C)}}\right)_{\mathrm{min}}^{\alpha(\mathrm{or}\ \gamma)}$. The formulation of $\left(u^{\mathrm{N(or\ C)}}\right)_{\mathrm{min}}^{\alpha(\mathrm{or}\ \gamma)}$ is derived in Appendix C. The values of $\left(u^{\mathrm{C}}\right)_{\mathrm{min}}^{\alpha}$, $\left(u^{\mathrm{N}}\right)_{\mathrm{min}}^{\alpha}$, $\left(u^{\mathrm{C}}\right)_{\mathrm{min}}^{\gamma}$, $\left(u^{\mathrm{N}}\right)_{\mathrm{min}}^{\gamma}$ are 3.05×10^{-5}, 7.9×10^{-6}, 0.02755 and 0.00247, respectively, at 930 K. The initial concentration of carbon in the α phase is fixed at 0.001, which leads to super-saturation of the carbon in the α phase, with $\Omega_{\mathrm{C}}^{\alpha} = 0.33\times10^{2}$. To ensure that the chemical kinetics drives the $\gamma\rightarrow\alpha$ transformation, the initial concentrations of carbon in the γ phase are set to be under-saturated, with $\left(u^{\mathrm{C}}\right)_{\mathrm{ini}}^{\gamma}$ = 0.01–0.015, i.e., $\Omega_{\mathrm{C}}^{\gamma}$ = 0.36–0.54. The initial nitrogen concentration in the α phase is 0.001 ($\Omega_{\mathrm{N}}^{\alpha} = 1.26\times10^{2}$), and varies in the γ phase varies from 0.01 to a very small value of 0.001 ($\Omega_{\mathrm{N}}^{\gamma} \approx 0.405$–$4.05$). It is noted that the Fe-C-N system can be conveniently reduced to an Fe-C system by ignoring the nitrogen concentration to the

chemical energy density. Thus, the comparison between Fe-C-N system and Fe-C system has also been implemented, where the Fe-C system is a special case achieved by setting the concentration of nitrogen in both the α and γ phases to 0 in the simulation.

Fig. 8

Figure 9(a) shows the variations of the tip radius against the initial concentrations of carbon and nitrogen in the γ phase. The tip curvature radius increases with the increasing initial values of Ω_C^γ and Ω_N^γ, because an increase in the initial concentration in the γ phase has a more significant effect at the tip than on the side. This is manifested by the variations in elemental accumulation, u_{max}, and diffusion length, l_{diff}, (see Fig. 4 for definitions) shown in Fig. 9(b). Figure 9(b) shows that u_{max}^N and l_{diff} increase with Ω_N^γ, and that the increases at the tip are more significant than those along the sides. The same trend can be observed for carbon diffusion (not shown). The elemental accumulation in front of the tip causes tip blunting, as shown in Fig. 9(a). More importantly, this accumulation explains why the tip observed in the Fe-C system is neither the sharpest nor the bluntest. In Fig. 9(a), it is noted that the curve pertaining to the Fe-C system is located between the two curves for $\Omega_N^\gamma > 1$ and $\Omega_N^\gamma < 1$. When the nitrogen concentration in the γ phase changes from super-saturation to under-saturation, the nitrogen diffusion from α to γ changes from being solely gradient-driven to being driven by both gradient and sink. In the latter case, tip sharpening increases with the degree of under-saturation (i.e., smaller Ω_N^γ).

While the effect of additional nitrogen diffusion on the tip radius is non-monotonic, the effect on the growth speed of the tip is straightforward, as shown in Fig. 9(c). In general, the addition of nitrogen reduces the tip velocity compared to the Fe-C system and the tip velocity decreases with Ω_N^γ, irrespective of under-saturation or super-saturation. This is because the tip velocity scales not only with the tip curvature, but also with the driving force, Δf, as expressed in Eq. (18). The chemical driving force at the Widmanstätten tip can be approximately expressed as follows:

$$\Delta f_{chem} = f_{chem}^{\gamma}\left(\left(u^{C}\right)^{\gamma},\left(u^{N}\right)^{\gamma},T\right) - f_{chem}^{\alpha}\left(\left(u^{C}\right)^{\alpha},\left(u^{N}\right)^{\alpha},T\right). \tag{20}$$

In Eq. (20), the effect of elemental accumulation is ignored owing to the low accumulation at the Widmanstätten tip as shown in Fig. 4(d). Letting $\left(u^{C(\text{or N})}\right)^{\alpha(\text{or }\gamma)} = \left(u^{C(\text{or N})}\right)_{ini}^{\alpha(\text{or }\gamma)}$, the resulting variation in Δf_{chem} is plotted against $\left(u^{N}\right)_{ini}^{\alpha}$ and $\left(u^{N}\right)_{ini}^{\gamma}$ in Fig. 9(d). For a given $\left(u^{N}\right)_{ini}^{\alpha}$, the chemical driven force always decreases monotonically with $\left(u^{N}\right)_{ini}^{\gamma}$, and the maximum Δf_{chem} occurs at zero nitrogen content in both phases.

Fig. 9

Finally, the effect of undercooling is examined. The velocity and radius of the Widmanstätten tip at different temperatures are shown in Fig. 10. The chemical driving force for the $\gamma \rightarrow \alpha$ transformation decreases monotonically from 457 J/mol to 276 J/mol with an increase in the temperature from 930K to 980K. As mentioned previously, the thickening of WF is dominated by the elemental diffusion, while the lengthening of WF is driven by the

mechanical and interfacial anisotropies, which are less affected by temperature. Elevation of the temperature leads to faster diffusion, which promotes the phase boundary migration more at the side than that at the tip. Consequently, the Widmanstätten tip becomes blunter with increasing temperature, as shown in Fig. 10.

Fig. 10

4. Conclusions

A phase field model for Widmanstätten ferrite formation is proposed to quantify the effects of interface anisotropy, misfit strain, and multicomponent diffusion, and is implemented in an Fe-C-N system with realistic thermodynamic parameters. Through parametric studies, the main findings can be summarized as follows:

(1) The individual effects of the interfacial anisotropy, misfit strain, and multicomponent diffusion are insufficient to explain the large aspect ratio of the Widmanstätten pattern observed experimentally. The Widmanstätten pattern is instead the result of their combined effects, which is not a simple linear superposition.

(2) The lengthening of the Widmanstätten plate has a constant velocity, which depends on the chemical driving force and the tip curvature. With increasing eigenstrain, anisotropic interfacial energy, degree of saturation in the γ phase, or degree of undercooling, the velocity of the Widmanstätten tip increases linearly. In contrast, the thickening is very slow, which is dominated by the diffusion rate.

(3) The Widmanstätten tip maintains a constant curvature during the transformation, which is independent of the initial morphology. The tip radius decreases with increasing eigenstrain, anisotropic interfacial energy, degree of under-saturation in the γ phase, or degree of undercooling.

Acknowledgments

This work was supported by the Early Career Scheme (ECS) of the Hong Kong Research Grants Council (Grant No. 25200515, Account F-PP27) and the Hong Kong Polytechnic University Departmental General Research Funds (G-YBMK). We are grateful for the support.

Appendix A

In present paper, the Fe-N-C solid solution phases are conceded. The chemical energy of the phase ρ with the formula $Fe_a(C,N,Va)_c$ per unit volume is expressed as:

$$f_{\text{chem}}^{\rho} = (y_{\text{C}}^{\rho}\,{}^{\text{o}}G_{\text{Fe:C}}^{\rho} + y_{\text{N}}^{\rho}\,{}^{\text{o}}G_{\text{Fe:N}}^{\rho} + y_{\text{va}}^{\rho}\,{}^{\text{o}}G_{\text{Fe:va}}^{\rho} + cRT\left[y_{\text{C}}^{\rho}\ln\left(y_{\text{C}}^{\rho}\right) + y_{\text{N}}^{\rho}\ln\left(y_{\text{N}}^{\rho}\right) + y_{\text{va}}^{\rho}\ln\left(y_{\text{va}}^{\rho}\right)\right] + G^{\rho,\text{ex}} + G^{\rho,\text{mag}})/V_{\text{m}}, \quad \text{(A.1)}$$

where y_{C}^{ρ}, y_{N}^{ρ} and y_{va}^{ρ} represent the fractions of sub-lattice occupancies of C, N, and Va, respectively. They satisfy the relationship that $1=y_{\text{C}}^{\rho}+y_{\text{N}}^{\rho}+y_{\text{va}}^{\rho}$ and can be expressed by u-function as $y_{\text{C(or N)}}^{\rho} = (\text{b}/\text{a})u^{\text{C(or N)}}$, where a and b are the site numbers of Fe and (C,N) atoms, respectively. They are defined as a=b=1 in the austenite and a=1, b=3 in the ferrite phase. ${}^{\text{o}}G_{\text{Fe:C}}^{\rho}$, ${}^{\text{o}}G_{\text{Fe:N}}^{\rho}$ and ${}^{\text{o}}G_{\text{Fe:va}}^{\rho}$ are the non-magnetic standard chemical energies per mole

for iron compounds, $G^{\rho,\mathrm{ex}}$ is the chemical energy per mole resulting from the interaction of second sub-lattices, $G^{\rho,\mathrm{mag}}$ is the magnetic contribution to the chemical energy density per mole, and V_m is the molar volume of substitutional atoms. Only considering binary interaction, $G^{\rho,\mathrm{ex}}$ is expressed as follows:

$$G^{\rho,\mathrm{ex}} = y_\mathrm{C}^\rho y_\mathrm{N}^\rho L_{\mathrm{Fe:C,N}}^\rho + y_\mathrm{C}^\rho y_\mathrm{va}^\rho L_{\mathrm{Fe:C,va}}^\rho + y_\mathrm{N}^\rho y_\mathrm{va}^\rho L_{\mathrm{Fe:N,va}}^\rho , \tag{A.2}$$

where $L_{\mathrm{Fe:C,N}}^\rho$, $L_{\mathrm{Fe:C,va}}^\rho$ and $L_{\mathrm{Fe:N,va}}^\rho$ are the binary interaction parameters. The realistic thermodynamic parameters from [23] are used in the present paper, as follow:

$$\begin{aligned} {}^\mathrm{o}G_\mathrm{Fe}^\alpha = {}^\mathrm{o}G_\mathrm{Fe:va}^\alpha = {} & 1224.83 + 124.134T - 23.5143T\ln T - \\ & 0.00439752T^2 - 5.89269\times10^{-8}T^3 + 77358.5T^{-1} , \end{aligned} \tag{A.3a}$$

$${}^\mathrm{o}G_\mathrm{Fe:C}^\alpha - {}^\mathrm{o}G_\mathrm{Fe}^\alpha = 322,050 + 75.665T , \tag{A.3b}$$

$${}^\mathrm{o}G_\mathrm{Fe:N}^\alpha - {}^\mathrm{o}G_\mathrm{Fe}^\alpha = 93,562 + 165.07T , \tag{A.3c}$$

$$L_\mathrm{Fe:C,va}^\alpha = -190T , \tag{A.3d}$$

$$G^{\alpha,\mathrm{mag}} = \begin{cases} -9180.5 + 9.723T - 9309.8\left(\dfrac{\tau^4}{6} + \dfrac{\tau^{10}}{135} + \dfrac{\tau^{16}}{600}\right), \tau < 1 \\ -6507.7\left(\dfrac{\tau^{-4}}{10} + \dfrac{\tau^{-14}}{315} + \dfrac{\tau^{-24}}{1500}\right), \tau \geq 1 \end{cases} , \tag{A.3e}$$

where τ=T/T_C and T_C=1043K is the Curie temperature. For γ phase the thermodynamic parameters are, as follows:

$$\begin{aligned} {}^\mathrm{o}G_\mathrm{Fe}^\gamma = {}^\mathrm{o}G_\mathrm{Fe:va}^\gamma = {} & -237.57 + 132.416T - 24.6643T\ln T - \\ & 0.00375752T^2 - 5.89269\times10^{-8}T^3 + 77358.5T^{-1} , \end{aligned} \tag{A.4a}$$

$${}^\mathrm{o}G_\mathrm{Fe:C}^\gamma - {}^\mathrm{o}G_\mathrm{Fe}^\gamma = 77,207 - 15.877T , \tag{A.4b}$$

$${}^\mathrm{o}G_\mathrm{Fe:N}^\gamma - {}^\mathrm{o}G_\mathrm{Fe}^\gamma = -20,277 + 245.3931T - 21.2984T\ln T , \tag{A.4c}$$

$$L_\mathrm{Fe:C,va}^\gamma = -34,671, \tag{A.4d}$$

$$L_\mathrm{Fe:N,va}^\gamma = -26,150, \tag{A.4e}$$

$$L_\mathrm{Fe:C,N}^\gamma = 8218, \tag{A.4f}$$

Based on Eq. (17, 19), the coefficient L_ki can be determined if the diffusional mobility M_ki^α and M_ki^γ is at hand. For the Fe-N-C solid solution, the diffusional mobility of carbon in

α and γ phase (mol·m^2/(J·s)), M_{CC}^{α} and M_{CC}^{γ}, can be obtained from [30], as follows:

$$RTM_{\mathrm{CC}}^{\alpha} = 2\times10^{-6}\mathrm{e}^{-10115/T}\exp\left\{0.5898\times\left[1+\frac{2}{\pi}\arctan\left(14.985-\frac{15309}{T}\right)\right]\right\}, \tag{A.5a}$$

$$RTM_{\mathrm{CC}}^{\gamma} = 4.529\times10^{-7}\exp\left[-\left(\frac{1}{T}-2.221\times10^{-4}\right)\times\left(17767-26436u^{\mathrm{C}}\right)\right]. \tag{A.5b}$$

The coefficient L_{ki} also can be determined from the diffusional coefficient, as follows:

$$D_{\mathrm{kj}} = \sum_{\mathrm{i}=1}^{\mathrm{n}} L_{\mathrm{ki}}\frac{\partial^2 f}{\partial u^{\mathrm{i}}\partial u^{\mathrm{j}}}, \tag{A.6}$$

If the cross diffusion is ignored, the coefficient L_{ki} could be simplified as $L_{\mathrm{ki}}=0$ ($\mathrm{k}\neq\mathrm{i}$). And L_{kk} can be expressed as follows:

$$L_{\mathrm{kk}} = \frac{D_{\mathrm{kk}}}{\left(\partial^2 f\big/\partial\left(u^{\mathrm{k}}\right)^2\right)}, \tag{A.7}$$

The diffusional coefficient of nitrogen in α and γ phase (m^2/s) can be obtained from [31][32], as follows:

$$D_{\mathrm{NN}}^{\alpha} = 0.464\times10^{-6}\exp\left(-10223.7/T\right), \tag{A.8a}$$

$$D_{\mathrm{NN}}^{\gamma} = 36.0\times10^{-6}\exp\left(-18883.8/T\right). \tag{A.8b}$$

Thus, the continual expression D_{NN} can be simply defined as follows:

$$D_{\mathrm{NN}} = \left(D_{\mathrm{NN}}^{\alpha}\right)^{p(\phi)}\left(D_{\mathrm{NN}}^{\gamma}\right)^{1-p(\phi)}. \tag{A.9}$$

Appendix B

The dimensionless government equation are, as follows:

$$\frac{\partial\phi}{\bar{M}_{\phi}\partial\bar{t}} = \left\{\begin{array}{l}\bar{\sigma}^0\bar{\delta}^0\left(\eta^2\bar{\nabla}^2\phi-\dfrac{\partial}{\partial\bar{x}}\left(\eta\eta'\dfrac{\partial\phi}{\partial\bar{y}}\right)+\dfrac{\partial}{\partial\bar{y}}\left(\eta\eta'\dfrac{\partial\phi}{\partial\bar{x}}\right)\right)- \\ \dfrac{\partial p(\phi)}{\partial\phi}\left(\bar{f}_{\mathrm{chem}}^{\alpha}+\bar{f}_{\mathrm{mech}}^{\alpha}-\bar{f}_{\mathrm{chem}}^{\gamma}-\bar{f}_{\mathrm{mech}}^{\gamma}\right)-\bar{W}\dfrac{\partial q(\phi)}{\partial\phi}\end{array}\right\}, \tag{B.1a}$$

$$\frac{\partial u^{\mathrm{k}}}{\partial\bar{t}} = \bar{\nabla}\cdot\left(u^{\mathrm{k}}y_{\mathrm{va}}\left(\begin{array}{l}\displaystyle\sum_{\mathrm{j}=1}^{\mathrm{n}}\sum_{\mathrm{i}=1}^{\mathrm{n}}\left(\bar{M}_{\mathrm{ki}}^{\alpha}\right)^{p(\phi)}\left(\bar{M}_{\mathrm{ki}}^{\gamma}\right)^{1-p(\phi)}\frac{\partial^2\bar{f}}{\partial u^{\mathrm{i}}\partial u^{\mathrm{j}}}\bar{\nabla}u^{\mathrm{j}}+ \\ \displaystyle\sum_{\mathrm{i}=1}^{\mathrm{n}}\left(\bar{M}_{\mathrm{ki}}^{\alpha}\right)^{p(\phi)}\left(\bar{M}_{\mathrm{ki}}^{\gamma}\right)^{1-p(\phi)}\frac{\partial^2\bar{f}}{\partial u^{\mathrm{i}}\partial\phi}\bar{\nabla}\phi\end{array}\right)\right) \tag{B.1b}$$

and

$$\mathrm{div}\left[\left(p(\phi)\bar{\mathbf{D}}_{\alpha}^{\mathrm{e}}+\left[1-p(\phi)\right]\bar{\mathbf{D}}_{\gamma}^{\mathrm{e}}\right)\left(\left\{\frac{1}{2}\left(\frac{\partial\bar{d}_i}{\partial\bar{x}_j}+\frac{\partial\bar{d}_j}{\partial\bar{x}_i}\right)\right\}-p(\phi)\boldsymbol{\varepsilon}^{\mathrm{g}}\right)\right]=0, \tag{B.1c}$$

respectively, where the variables and parameters with the over-head bar are defined as $\bar{M}_{\phi}=\left(M_{\phi}l^{2}\right)/\left(M_{\mathrm{CC}}^{\alpha}\right)$, $\bar{\sigma}^{0}=\sigma^{0}/\left(lRT\right)$, $\bar{\delta}^{0}=\delta^{0}/l$, $\bar{f}^{\alpha(\mathrm{or}\,\gamma)}=\left(f^{\alpha(\mathrm{or}\,\gamma)}\right)/\left(V_{\mathrm{m}}RT\right)$, $\bar{W}=W/\left(V_{\mathrm{m}}RT\right)$, $\left(\bar{M}_{\mathrm{ki}}^{\alpha}\right)^{p(\phi)}\left(\bar{M}_{\mathrm{ki}}^{\gamma}\right)^{1-p(\phi)}=\left(M_{\mathrm{ki}}^{\alpha}\right)^{p(\phi)}\left(M_{\mathrm{ki}}^{\gamma}\right)^{1-p(\phi)}/M_{\mathrm{CC}}^{\alpha}$ and $\bar{\mathbf{D}}_{\alpha(\mathrm{or}\,\gamma)}^{\mathrm{e}}=\mathbf{D}_{\alpha(\mathrm{or}\,\gamma)}^{\mathrm{e}}/\left(V_{\mathrm{m}}RT\right)$.

Appendix C

Substituting the Eq. (A.2) into Eq. (A.1), the chemical energy density of phase ρ is expressed as follows:

$$f_{\mathrm{chem}}^{\rho}=\left(y_{\mathrm{C}}^{\rho}\,{}^{\mathrm{o}}G_{\mathrm{Fe:C}}^{\rho}+y_{\mathrm{N}}^{\rho}\,{}^{\mathrm{o}}G_{\mathrm{Fe:N}}^{\rho}+y_{\mathrm{va}}^{\rho}\,{}^{\mathrm{o}}G_{\mathrm{Fe:va}}^{\rho}+cRT\left[y_{\mathrm{C}}^{\rho}\ln\left(y_{\mathrm{C}}^{\rho}\right)+y_{\mathrm{N}}^{\rho}\ln\left(y_{\mathrm{N}}^{\rho}\right)+y_{\mathrm{va}}^{\rho}\ln\left(y_{\mathrm{va}}^{\rho}\right)\right]+\right.$$
$$\left.y_{\mathrm{C}}^{\rho}y_{\mathrm{N}}^{\rho}L_{\mathrm{Fe:C,N}}^{\rho}+y_{\mathrm{C}}^{\rho}y_{\mathrm{va}}^{\rho}L_{\mathrm{Fe:C,va}}^{\rho}+y_{\mathrm{N}}^{\rho}y_{\mathrm{va}}^{\rho}L_{\mathrm{Fe:N,va}}^{\rho}+G^{\rho,\mathrm{mag}}\right)/V_{\mathrm{m}} \quad , \quad \text{(C.1)}$$

Due to the fact that y_{C}^{ρ}, y_{N}^{ρ} are quite small, $y_{\mathrm{C}}^{\rho}y_{\mathrm{N}}^{\rho}$ is assumed to be the high-order minim and $\ln(y_{\mathrm{va}}^{\rho})$ is approximately expressed as $\ln(y_{\mathrm{va}}^{\rho})=(-y_{\mathrm{C}}^{\rho}-y_{\mathrm{N}}^{\rho})$. As the consequence, the chemical energy density of phase ρ f_{chem}^{ρ} can be approximately expressed as follows:

$$f_{\mathrm{chem}}^{\rho}\approx\left(y_{\mathrm{C}}^{\rho}\,{}^{\mathrm{o}}G_{\mathrm{Fe:C}}^{\rho}+y_{\mathrm{N}}^{\rho}\,{}^{\mathrm{o}}G_{\mathrm{Fe:N}}^{\rho}+\left(1-y_{\mathrm{C}}^{\rho}-y_{\mathrm{N}}^{\rho}\right)\,{}^{\mathrm{o}}G_{\mathrm{Fe:va}}^{\rho}+\right)$$
$$cRT\left[y_{\mathrm{C}}^{\rho}\ln\left(y_{\mathrm{C}}^{\rho}\right)+y_{\mathrm{N}}^{\rho}\ln\left(y_{\mathrm{N}}^{\rho}\right)+\left(-y_{\mathrm{C}}^{\rho}-y_{\mathrm{N}}^{\rho}\right)\right]+. \quad \text{(C.2)}$$
$$\left.y_{\mathrm{C}}^{\rho}L_{\mathrm{Fe:C,va}}^{\rho}+y_{\mathrm{N}}^{\rho}L_{\mathrm{Fe:N,va}}^{\rho}+G^{\rho,\mathrm{mag}}\right)/V_{\mathrm{m}}$$

In this case, the partial derivative of f_{chem}^{ρ} with respect to variable y_{C}^{ρ} and y_{N}^{ρ}, can be derived as follows:

$$\frac{\partial f_{\mathrm{chem}}^{\rho}}{\partial y_{\mathrm{C}}^{\rho}}\approx\left({}^{\mathrm{o}}G_{\mathrm{Fe:C}}^{\rho}-{}^{\mathrm{o}}G_{\mathrm{Fe:va}}^{\rho}+cRT\ln\left(y_{\mathrm{C}}^{\rho}\right)+L_{\mathrm{Fe:C,va}}^{\rho}\right)/V_{\mathrm{m}} \quad \text{(C.3a)}$$

and $\frac{\partial f_{\mathrm{chem}}^{\rho}}{\partial y_{\mathrm{N}}^{\rho}}\approx\left({}^{\mathrm{o}}G_{\mathrm{Fe:N}}^{\rho}-{}^{\mathrm{o}}G_{\mathrm{Fe:va}}^{\rho}+cRT\ln\left(y_{\mathrm{N}}^{\rho}\right)+L_{\mathrm{Fe:N,va}}^{\rho}\right)/V_{\mathrm{m}}$, respectively. (C.3b)

When $\partial f_{\mathrm{chem}}^{\rho}/\partial y_{\mathrm{C}}^{\rho}$ and $\partial f_{\mathrm{chem}}^{\rho}/\partial y_{\mathrm{N}}^{\rho}$ are set to be zero, the minimum value $y_{\mathrm{C}\min}^{\rho}$ and $y_{\mathrm{N}\min}^{\rho}$ can be, respectively, derived as follows:

$$y_{\mathrm{C}\min}^{\rho}\approx\exp\left(\frac{{}^{\mathrm{o}}G_{\mathrm{Fe:va}}^{\rho}-{}^{\mathrm{o}}G_{\mathrm{Fe:C}}^{\rho}-L_{\mathrm{Fe:C,va}}^{\rho}}{cRT}\right)\ \text{and}\ y_{\mathrm{N}\min}^{\rho}\approx\exp\left(\frac{{}^{\mathrm{o}}G_{\mathrm{Fe:va}}^{\rho}-{}^{\mathrm{o}}G_{\mathrm{Fe:N}}^{\rho}-L_{\mathrm{Fe:N,va}}^{\rho}}{cRT}\right). \quad \text{(C.4)}$$

Since $y_{\mathrm{C}}^{\alpha}=1/3u^{\mathrm{C}}$, $y_{\mathrm{N}}^{\alpha}=1/3u^{\mathrm{N}}$, $y_{\mathrm{C}}^{\gamma}=u^{\mathrm{C}}$ and $y_{\mathrm{N}}^{\gamma}=u^{\mathrm{N}}$, the minimum u-fraction of carbon and nitrogen in α and γ phase can be, respectively, expressed as follows:

$$\left(u^{\mathrm{C}}\right)_{\min}^{\alpha}\approx\frac{1}{3}\exp\left(\frac{{}^{\mathrm{o}}G_{\mathrm{Fe:va}}^{\rho}-{}^{\mathrm{o}}G_{\mathrm{Fe:C}}^{\rho}-L_{\mathrm{Fe:C,va}}^{\rho}}{3RT}\right),\ \left(u^{\mathrm{N}}\right)_{\min}^{\alpha}\approx\frac{1}{3}\exp\left(\frac{{}^{\mathrm{o}}G_{\mathrm{Fe:va}}^{\rho}-{}^{\mathrm{o}}G_{\mathrm{Fe:N}}^{\rho}-L_{\mathrm{Fe:N,va}}^{\rho}}{3RT}\right), \quad \text{(C.5a)}$$

$$\left(u^{\mathrm{C}}\right)^{\gamma}_{\min} \approx \exp\left(\frac{{}^{\mathrm{o}}G^{\rho}_{\mathrm{Fe:va}} - {}^{\mathrm{o}}G^{\rho}_{\mathrm{Fe:C}} - L^{\rho}_{\mathrm{Fe:C,va}}}{RT}\right) \text{ and } \left(u^{\mathrm{N}}\right)^{\gamma}_{\min} \approx \exp\left(\frac{{}^{\mathrm{o}}G^{\rho}_{\mathrm{Fe:va}} - {}^{\mathrm{o}}G^{\rho}_{\mathrm{Fe:N}} - L^{\rho}_{\mathrm{Fe:N,va}}}{RT}\right). \quad \text{(C.5b)}$$

References

[1] C. Zener, Kinetics of the decomposition of austenite, Trans. Am. Inst. Min. Metall. Eng. 167(1946) 550-595.

[2] M. Hillert, L. Höglund, J. Ågren, Diffusion-controlled lengthening of Widmanstätten plates, Acta Mater. 51(2003) 2089-2095.

[3] R. Trivedi, The role of interfacial free energy and interface kinetics during the growth of precipitate plates and needles, Metall. Trans. 1(1970) 921-927.

[4] R.D. Townsend, J.S. Kirkaldy, Widmanstaetten ferrite formation in Fe-C alloys, ASM. Trans. Quart. 61(1968) 605-619.

[5] W.W. Mullins, R.F. Sekerka, Morphological stability of a particle growing by diffusion or heat flow, J. Appl. Phys. 34(1963) 323-329.

[6] L.Q. Chen, A.G. Khachaturyan, Computer simulation of structural transformations during precipitation of an ordered intermetallic phase, Acta Metall. Mater. 39(1991) 2533-2551.

[7] X. Zhang, H.F Wang, W.W Kuang, J.B. Zhang, Application of the thermodynamic extremal principle to phase-field modeling of non-equilibrium solidification in multi-component alloys, Acta Mater. 128(2017) 258-269.

[8] K. Grönhagen, J. Ågren, M. Odén, Phase-field modelling of spinodal decomposition in TiAlN including the effect of metal vacancies, Scripta Mater. 95(2015) 42-45.

[9] D. Tourret, Y. Song, A.J. Clarke, A. Karma, Grain growth competition during thin-sample directional solidification of dendritic microstructures: A phase-field study, Acta Mater. 122(2017) 220-235.

[10] J.A. Stewart, D.E. Spearot, Phase-field simulations of microstructure evolution during physical vapor deposition of single-phase thin films, Comp. Mater. Sci. 131(2017) 170-177.

[11] L. Chen, J. Chen, R.A. Lebensohn, Y.Z. Ji, T.W. Heo, S. Bhattacharyya, K. Chang, S. Mathaudhu, Z.K. Liu, L.Q. Chen, An integrated fast fourier transform-based phase-field and crystal plasticity approach to model recrystallization of three dimensional polycrystals, Comput. Methods Appl. Mech. Eng. 285(2015) 829-848.

[12] H.S. Udaykumar, L. Mao, R. Mittal, A finite-volume sharp interface scheme for dendritic growth simulations: comparison with microscopic solvability theory, Numer. Heat. Tr B-fund. 42 (2002) 389-409.

[13] I. Loginova, J. Ågren, G. Amberg, On the formation of Widmanstätten ferrite in binary Fe-C-phase-field approach, Acta Mater. 52(2004) 4055-4063.

[14] A. Yamanaka, T. Takaki, Y. Tomita, Phase-Field Simulation of Austenite to Ferrite Transformation and Widmanstätten Ferrite Formation in Fe-C Alloy, Mater. Trans. 47(2006) 2725-2731.

[15] L. Thuinet, A. De Backer, A. Legris, Phase-field modeling of precipitate evolution dynamics in elastically inhomogeneous low-symmetry systems: application to hydride precipitation in Zr, Acta Mater. 60(2012) 5311-5321.

[16] G. Boussinot, Y. Le Bouar, A. Finel, Phase-field simulations with inhomogeneous elasticity: Comparison with an atomic-scale method and application to superalloys, Acta Mater. 58(2010) 4170-4181.
[17] M. Cottura, B. Appolaire, A. Finel, Y. Le Bouar, Phase field study of acicular growth: role of elasticity in Widmanstatten structure, Acta Mater. 72(2014) 200-210.
[18] M. Cottura, B. Appolaire, A. Finel, Y. Le Bouar, Plastic relaxation during diffusion-controlled growth of Widmanstätten plates, Scripta Mater. 108(2015) 117-121.
[19] L. Zhang, Y. Shen, H. Wan, X. Xiong, L. Zhang, The study of Widmanstätten ferrite in Fe-C alloys by a phase field model coupled with anisotropic elasticity, J. Alloy Compd. 650(2015) 239-247.
[20] V. Ginzburg, L. Landau, On the theory of superconductivity, Zh. Eksp.Teor. Fiz. 20 (1950) 1064–1082. Translation in Collected papers of L.D.Landau, Pergamon, Oxford, 1965, pp. 546-568.
[21] S.G. Kim, W.T. Kim, T. Suzuki, Interfacial compositions of solid and liquid in a phase-field model with finite interface thickness for isothermal solidification in binary alloys, Phys. Rev. E 58(1998) 3316.
[22] K. Ammar, B. Appolaire, G. Cailletaud, F. Frederic, F. Samuel, Finite element formulation of a phase field model based on the concept of generalized stresses, Comp. Mater. Sci. 45(2009) 800-805.
[23] H. Göhring, O. Fabrichnaya, A. Leineweber, E.J. Mittemeijer, Thermodynamics of the Fe-N and Fe-N-C Systems: The Fe-N and Fe-N-C Phase Diagrams Revisited, Metallurgical & Materials Transactions A, 47(2016) 6173-6186.
[24] S. M. Allen, J. W. Cahn, A microscopic theory for antiphase boundary motion and its application to antiphase domain coarsening, Acta Metall. 27(1979) 1085-1095.
[25] L. Onsager, S. Machlup, Fluctuations and irreversible processes, Phys. Rev. 91(1953) 1505.
[26] COMSOL Multiphysics Users' Guide. Available from: http://www.comsol.com/.
[27] M. Hillert, G.R. Purdy. Chemically induced grain boundary migration, Acta Metall. 26(1978) 333-340.
[28] G.B. Mcfadden, A.A. Wheeler, R.J. Braun, S.R. Coriell, R.F. Sekerka, Phase-field models for anisotropic interfaces, Phys. Rev. E, 48(1993) 2016.
[29] M. Enomoto, Thermodynamics and kinetics of the formation of Widmanstätten ferrite plates in ferrous alloys, Metall. Mater. Trans. A 25(1994) 1947-1955.
[30] P. Gustafson, Thermodynamic evaluation of the Fe-C system, Scand. J Metall. 14(1985) 259-267.
[31] S. Hertzman, B. Brolund, P.J. Ferreira, An experimental and theoretical study of heat-affected zone austenite reformation in three duplex stainless steels, Metall. Mater. Trans. A 28(1997) 277-285.
[32] G. Engberg, M. Hillert, A. Oden, Estimation of the rate of diffusion-controlled growth by means of a quasi-stationary model, Scand. J Metall. 4(1975) 93-96.

Tables

Table 1 Material properties used in present phase field model

	Parameter	Value
Interface mobility [27]	M (m^4/J/s)	0.035exp(-17700/T)
Coefficient of interface mobility [13]	ς	0.235
Interfacial energy density	σ_0 (J/ m^2)	1
Interface thickness	δ_0 (nm)	10
Young's Module for α and γ phase	E (GPa)	130
Poisson ratio for α and γ phase	v	0.3
Molar volume of substitutional atoms	V_m (m^3/mol)	7×10^{-6}
Ideal gas constant	R (J/mol/K)	8.314

Figures Captain

Fig. 1. The geometry and boundary condition of the phase field simulation.

Fig. 2. The counter plot of Widmanstätten ferrite after 1200μs at 930K (a) considering interfacial anisotropy and misfit strain, (b) only the interfacial anisotropy and (c) only the misfit strain.

Fig. 3. (a, b) The distributions of elastic energy along the Y and X directions, and (c) the evolutions of elastic energies at the Widmanstätten tip and side.

Fig. 4. (a, b) The distributions of carbon and nitrogen along Y and X axes at 300μs, and (c, d) the evolutions of diffusion length and elemental accumulation with time.

Fig. 5. (a) The lengthening and (b) thickening of Widmanstätten ferrite with time, where H and W are the lengthening and thickening values, respectively.

Fig. 6. The tip curvature radius r with different initial morphologies.

Fig. 7. (a) The curvature radius r and (b) the velocity v_n^{tip} with eigenstrain ε_{11}^g and anisotropic interfacial energy strength a.

Fig. 8. The diagrammatic sketch of the chemical energy density for the Fe-C-N solid solution for α and γ phase.

Fig. 9. (a) the evolution of tip curvature radius with Ω_C^γ and Ω_N^γ, (b) the diffusion length l_{diff} and elemental accumulation of carbon u_{max}^N at 300μs with the different Ω_N^γ, (c) the evolution of Widmanstätten tip velocity with Ω_C^γ and Ω_N^γ, and (d) the evolution of Δf_{chem} with initial concentration of nitrogen in γ phase.

Fig. 10. The Widmanstätten tip velocity and the curvature radius with temperature.

Highlights

- Phase field model for Widmanstätten formation in steel is proposed.
- Interfacial anisotropy, misfit strain and multicomponent are considered.
- Widmanstätten tip velocity and curvature are investigated.

Figure 1
Click here to download high resolution image

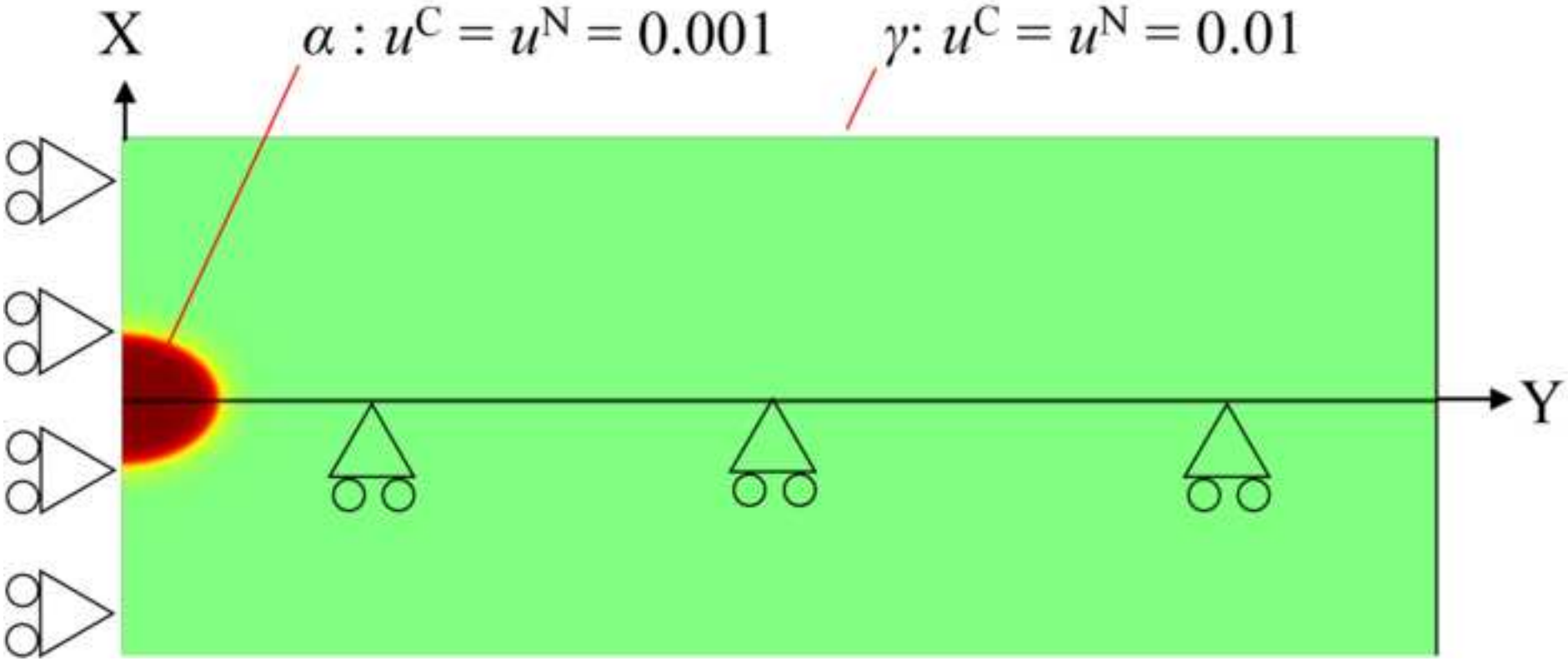

Figure 2

Click here to download high resolution image

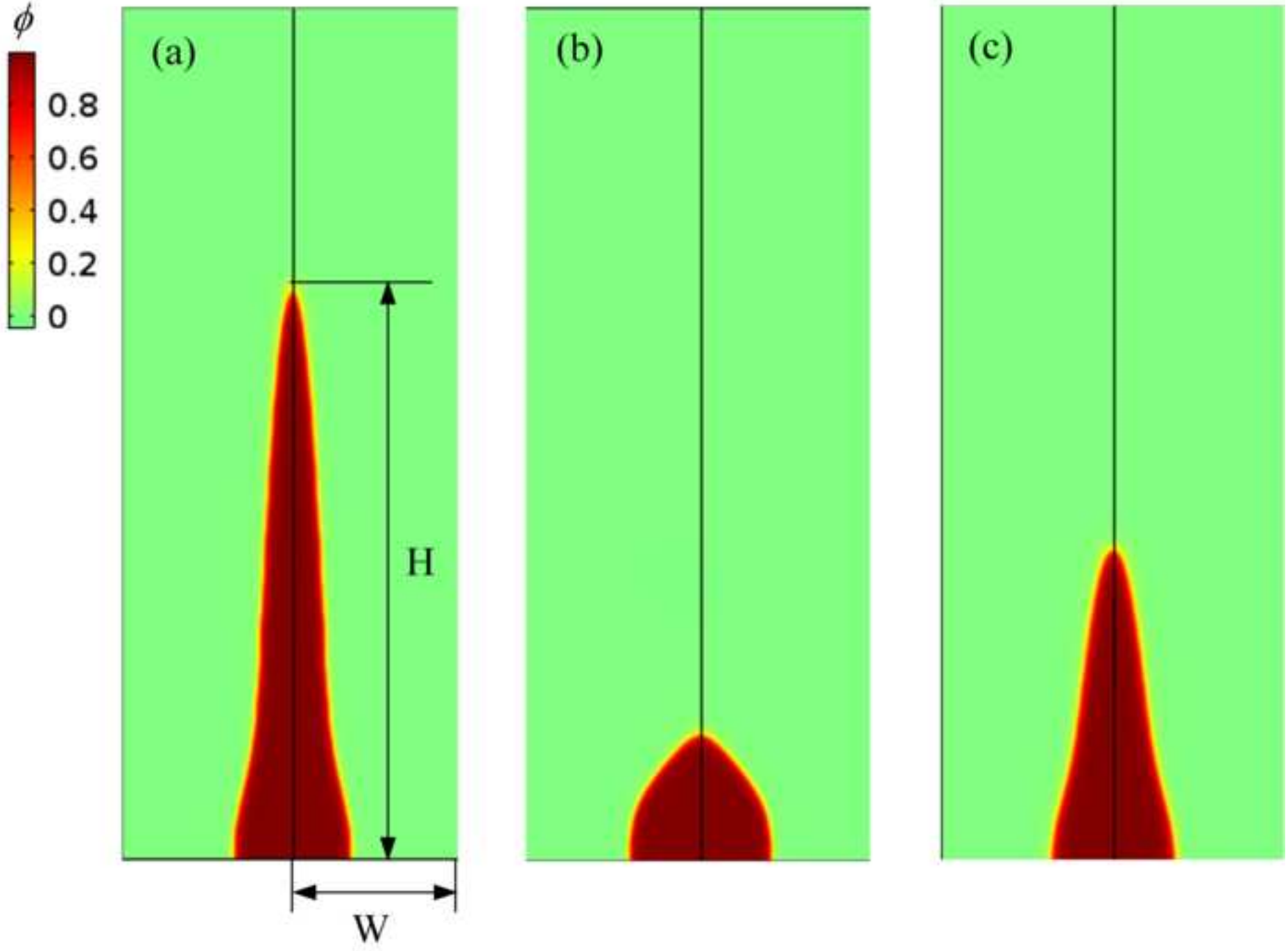

Figure 3

Click here to download high resolution image

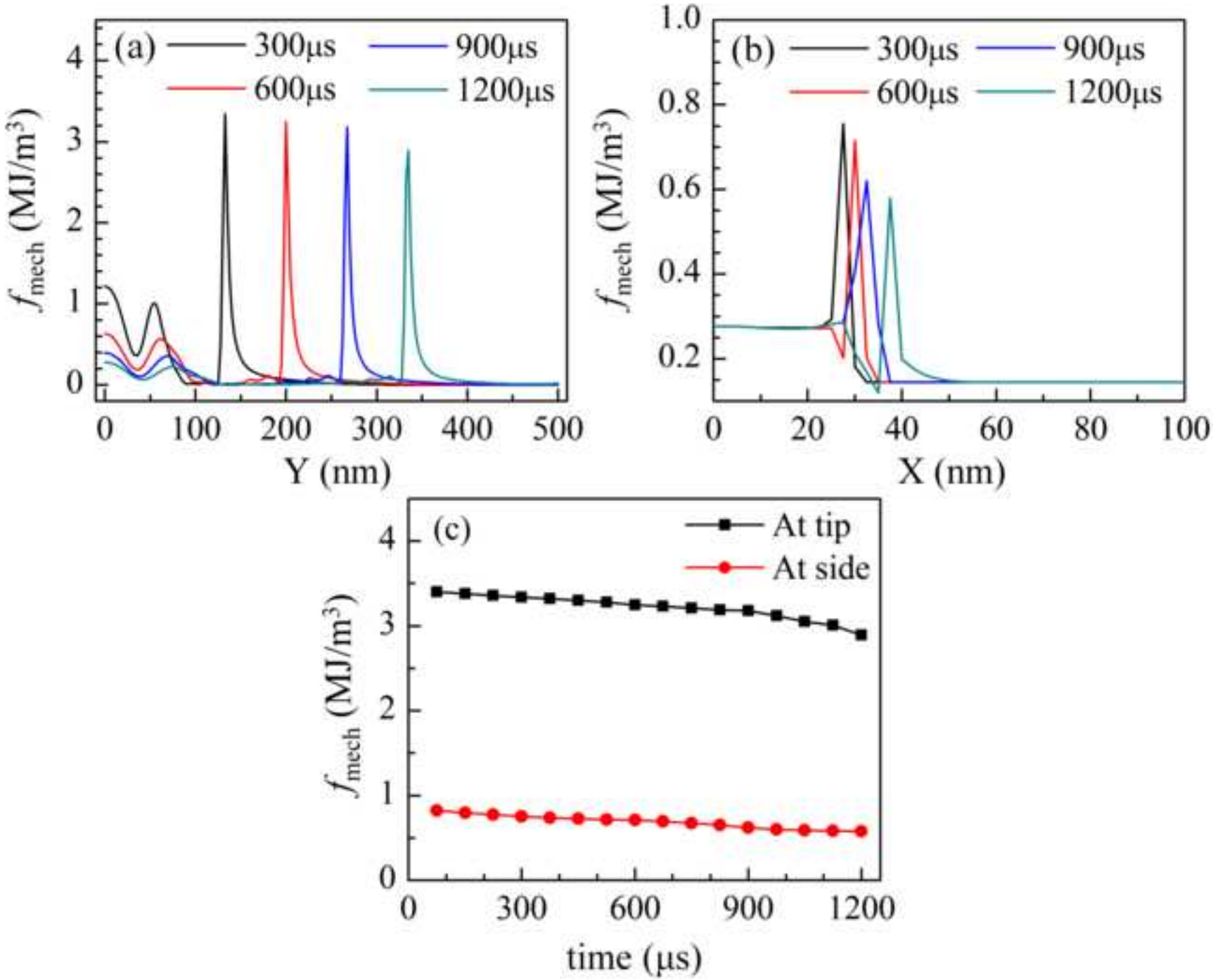

Figure 4

Click here to download high resolution image

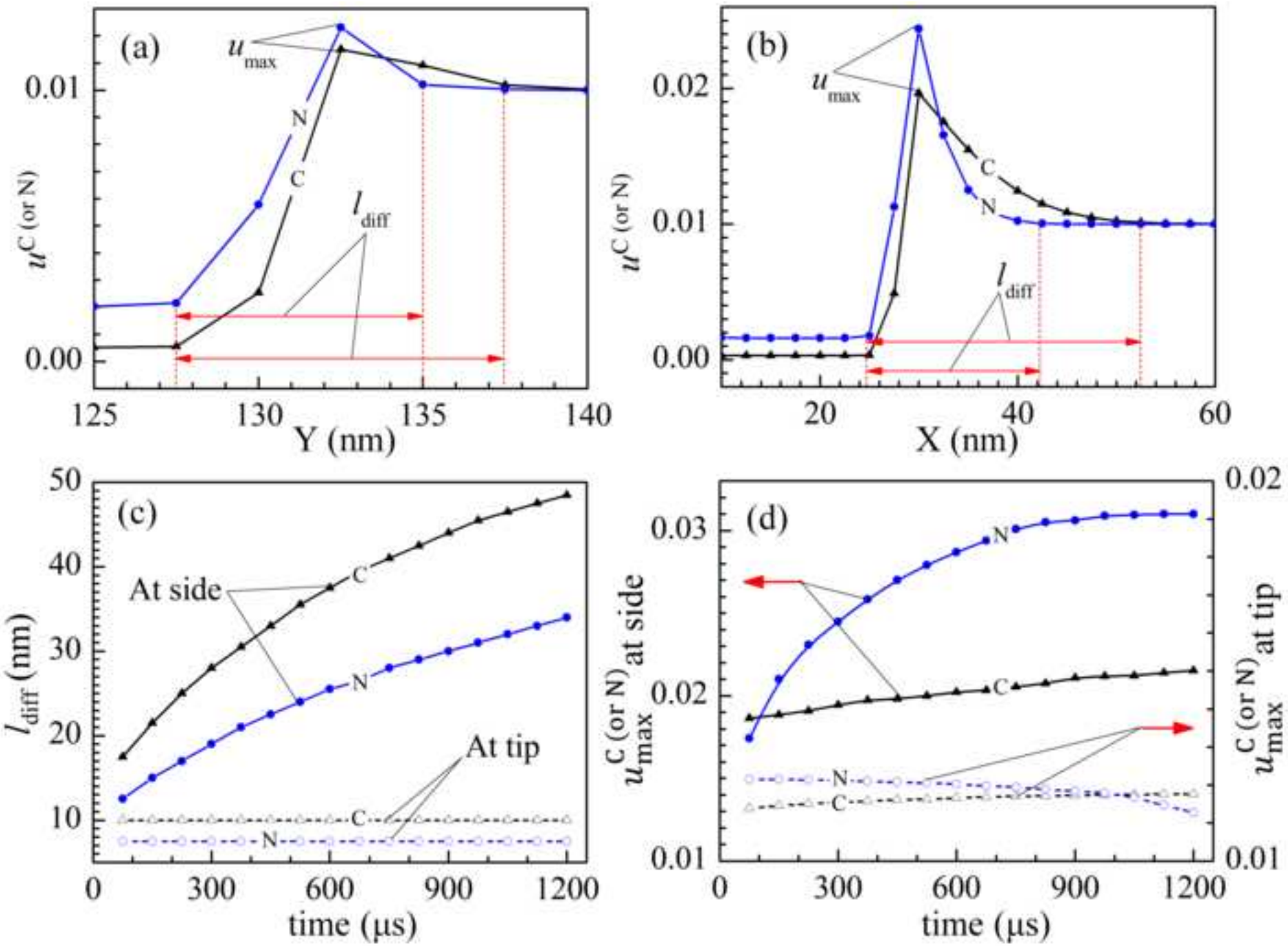

Figure 5

Click here to download high resolution image

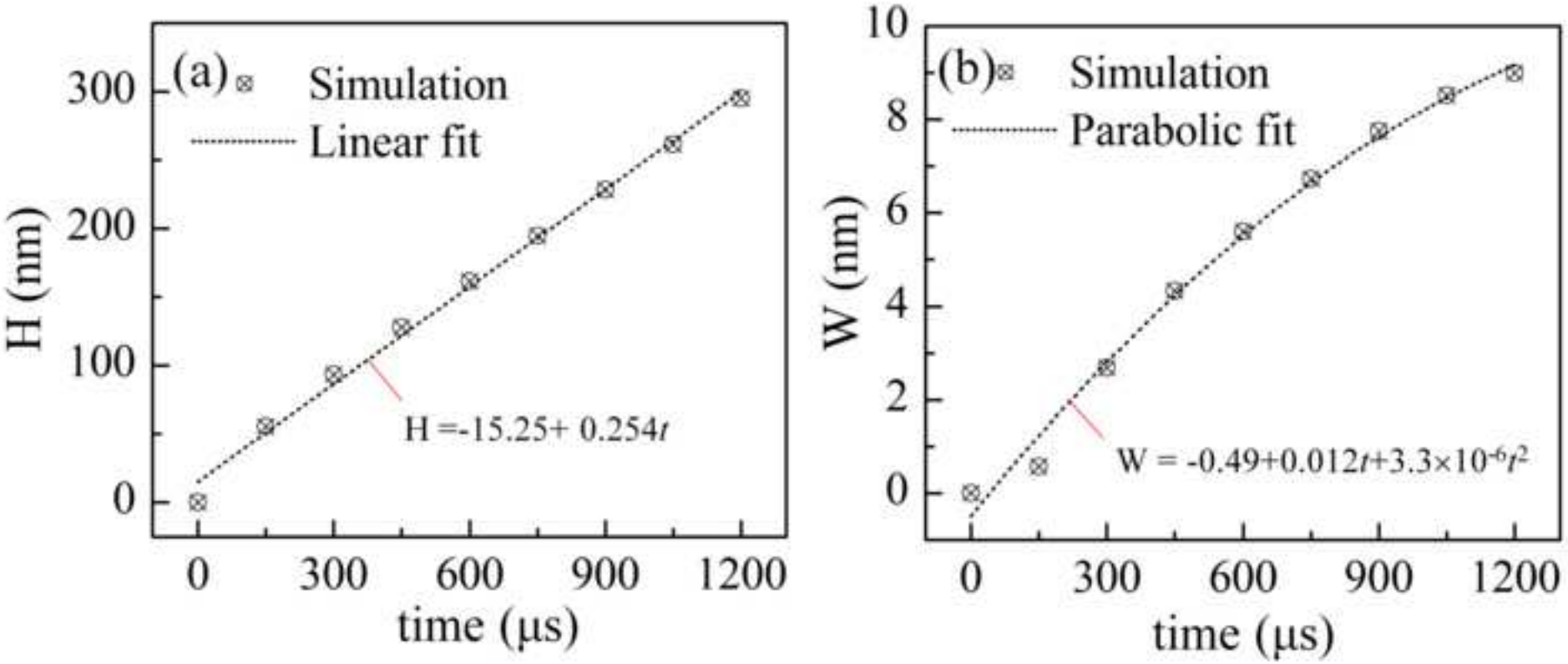

Figure 6

Click here to download high resolution image

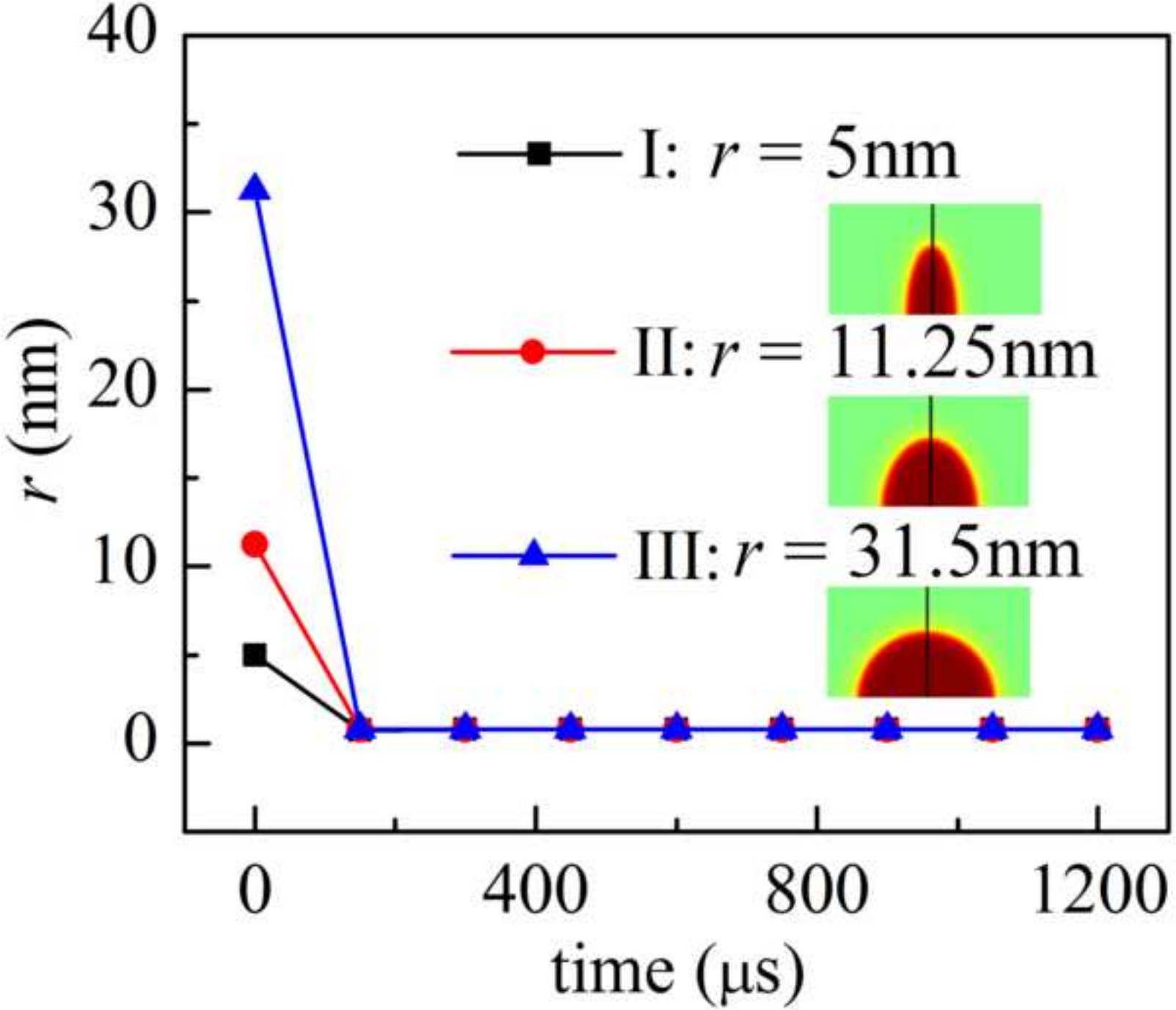

Figure 7

Click here to download high resolution image

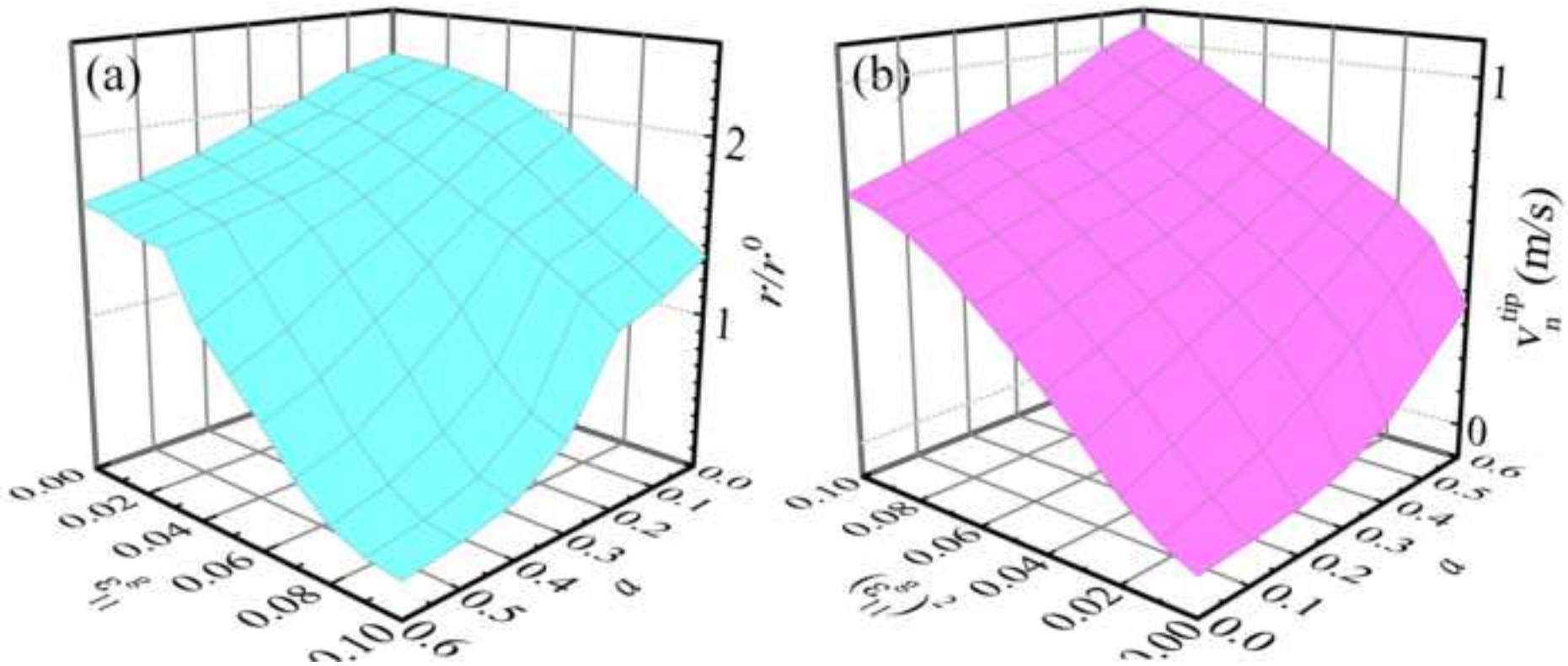

Figure 8

Click here to download high resolution image

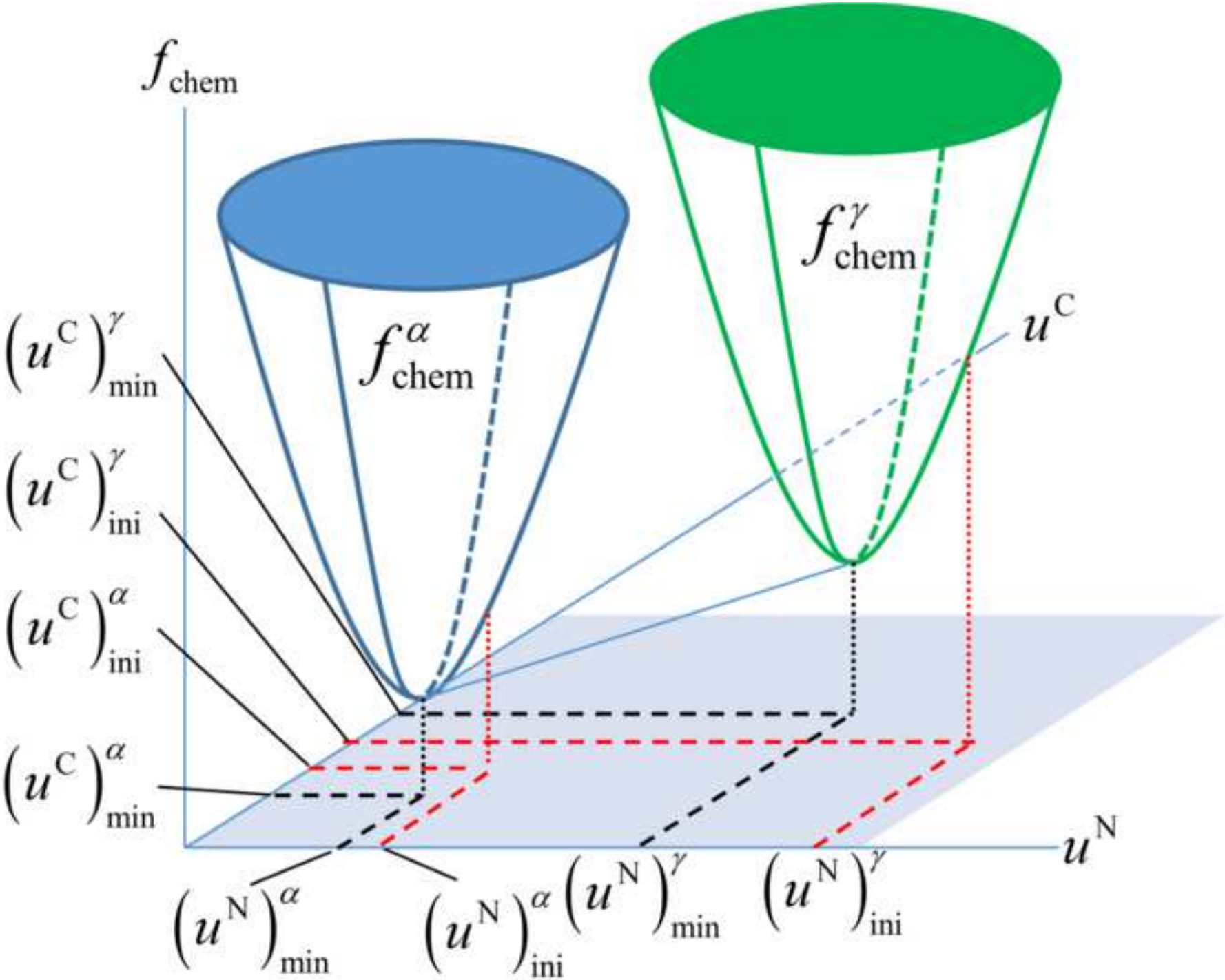

Figure 9

Click here to download high resolution image

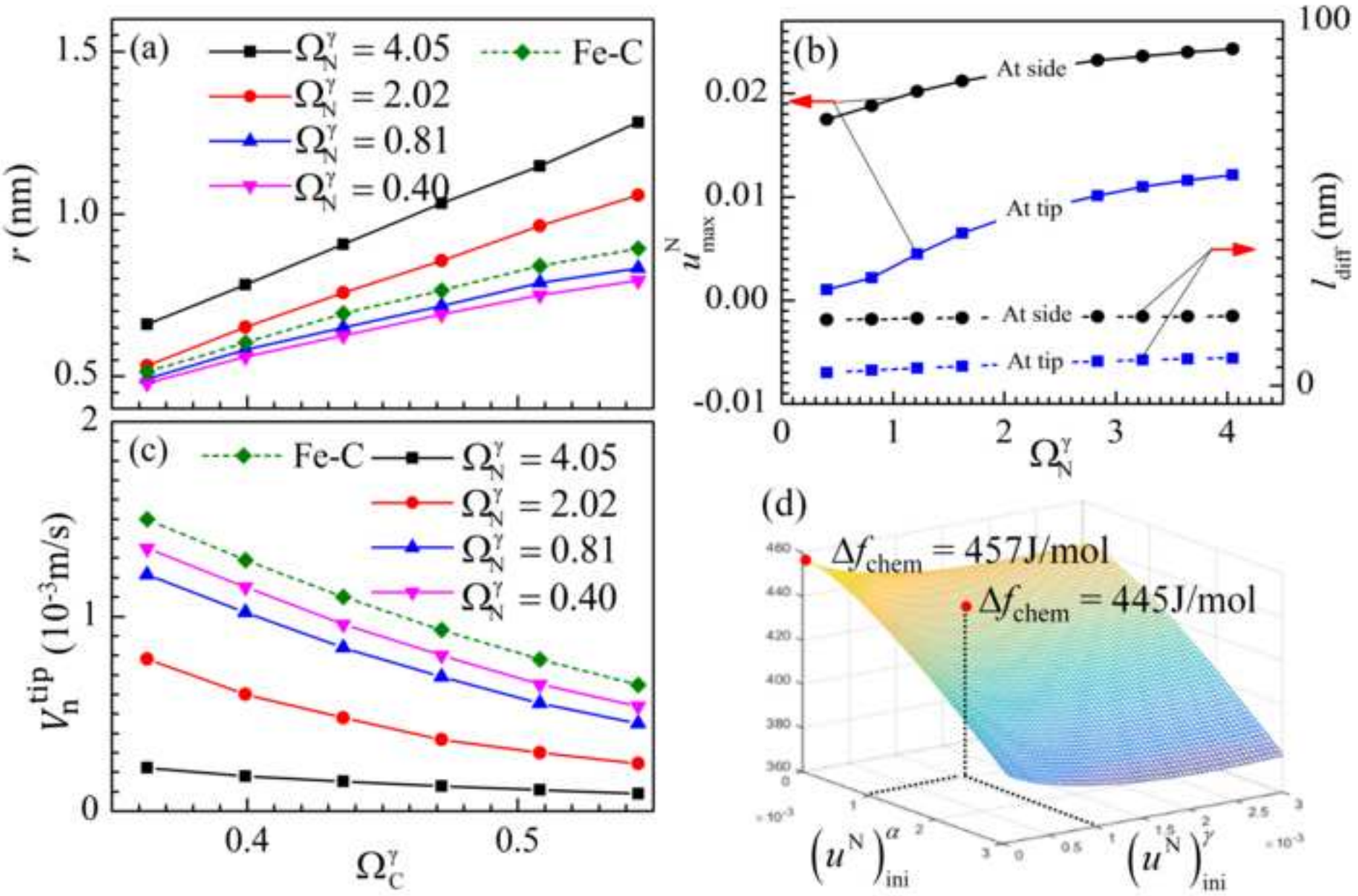

Figure 10

Click here to download high resolution image